

Title

Broadband *unidirectional guided-wave*-driven metasurfaces for arbitrary wavefront control

Authors

Shiqing Li¹, Kosmas L. Tsakmakidis^{2*}, Qian Shen¹, Hang Zhang¹, Jinhua Yan¹, Shulin Sun³, Linfang Shen^{1*}

*Corresponding authors: Linfang Shen, lfshen@zjut.edu.cn; Kosmas L. Tsakmakidis, ktsakmakidis@phys.uoa.gr.

Affiliations

¹Department of Applied Physics, Zhejiang University of Technology, Hangzhou 310023, China.

²Section of Condensed Matter Physics, Department of Physics, National and Kapodistrian University of Athens Panepistimioupolis, Athens GR-157 84, Greece.

³Shanghai Engineering Research Centre of Ultra Precision Optical Manufacturing, Department of Optical Science and Engineering, School of Information Science and Technology, Fudan University, Shanghai 200433, China.

Abstract

Metasurfaces, composed of subwavelength microstructures, known as meta-atoms, are capable of reshaping the wavefronts of incident beams in desired manners, making them great candidates for revolutionizing conventional optics. However, the requirement for external light excitation and the resonant nature of meta-atoms make it difficult to fully integrate metasurfaces on-chip, or to control wavefronts at *deep-subwavelength* scales. Here, we introduce the concept and design of a new type of a metasurface, driven by *unidirectional* guided waves rather than bi-directional resonant meta-atoms, being capable of arbitrary wavefront control by harnessing the unique properties of *unidirectional* guided waves. We numerically demonstrate this new principle through the design of several microwave meta-devices using unidirectional surface magnetoplasmans, agilely converting unidirectional guided modes into wavefronts of bessel beams, 3D focused waves, and controllable vortex beams. Based on this *nonresonant* (i.e., broadband) mechanism and on monolithically integrated magneto-optical platforms, our metasurfaces may conceivably open new vistas for applications in communications, remote sensing, displays and holography.

Teaser

Our research introduces a novel class of metasurfaces that utilize *unidirectional guided waves* (rather than bi-directional resonant meta-atoms) to enable arbitrary control over free-space electromagnetic waves by directly extracting guided waves from their propagation into free space and molding them into desired light wavefronts. These metasurfaces do not need standard meta-atoms to induce abrupt phase shifts, and can manipulate electromagnetic waves at deep-subwavelength scales. The presented technology opens up new possibilities for applications in various fields, such as communications, remote sensing, and virtual reality displays.

MAIN TEXT

Introduction

Light can be confined at the nanoscale through the coupling with surface plasmon polaritons (SPPs) (1). The two-dimensional nature of SPPs offers significant flexibility in engineering photonic integrated circuits for optical communications and optical computing (2-4). However, the backscattering of SPPs by disorders, due to the reciprocity of plasmonic platforms, limits their applications in optical devices. Developing nonreciprocal plasmonic platforms (5) that enable unidirectional SPP propagation is, therefore, of great importance. Such unidirectional SPPs occur in topologically nontrivial systems made of nonreciprocal materials, where the magnetic field breaks time-reversal symmetry, are known as unidirectional surface magnetoplasmons (USMPs) (6-14). These USMPs are immune to backscattering at disorders, making them ideal for realizing new classes of optical devices that are impossible using conventional reciprocal modes, such as optical cavities that overcome the time-bandwidth limit [Science 356, 1260 (2017)] (15).

On the other hand, newly emerging metasurfaces (16-18) can provide unparalleled control over electromagnetic (EM) waves to realize complex free-space functions, such as beam deflection (19, 20), focusing (21-23), generation of orbital angular momentum beams (24), and holograms (25). Metasurfaces rely on engineered optical resonators known as meta-atoms, which locally provide abrupt phase shifts at subwavelength intervals to tailor the phase of incident waves, making them exhibit predetermined functions for transmitted or reflected waves based on the Huygens principle. However, most metasurfaces are driven by free-space waves, making their on-chip integration challenging. Moreover, based on the resonant mechanism of the meta-atoms, the designed wavelengths of metasurfaces are closely related to the sizes of the meta-atoms, making it difficult to shape wavefronts on deep subwavelength scales. These metasurfaces also generally operate within a narrow frequency range.

It is interesting if USMP could offer a completely new mechanism for metasurfaces that has no resonant nature. USMPs, relying on the band gap of nonreciprocal materials themselves, easily attain broad bandwidth and exhibit striking dispersion properties. For example, in the microwave range, the dispersion curve of USMPs in yttrium-iron-garnet (YIG) can monotonically grow across the entire light cone in air. Thus, USMPs can smoothly convert from forward wave to backward wave without any frequency gap. As the dispersion of USMPs is closely related to the structural details and, hence, can be flexibly tailored through controlling the structural parameters. For USMPs at a fixed frequency, the phase constant can be tuned over the range $[-k_0, k_0]$ (where k_0 is the free-space wavenumber). Based on this unparalleled phase controllability, here we develop a new class of metasurfaces that are driven by USMPs to realize complex free-space functions (Fig. 1). The subwavelength-sized unit cells of USMP-driven metasurfaces support two types of USMPs, and the conversion between them creates a directional radiation that extracts guided waves into free space and molds them into desired light fields. Based on the robustness of USMPs, the proposed metasurfaces would be utterly immune to both back scattering and surface-roughness scattering. Besides, multiple metasurfaces can be directly connected to achieve different free-space functions simultaneously.

In contrast to existing guide wave-driven metasurfaces (26-28), our USMP-driven metasurfaces provide desired spatial phase profiles for extracted waves directly from the propagation of USMPs, thus do not need any meta-atoms to induce abrupt phase shifts. Although plasmonic metasurfaces based on Bragg interferences also work without meta-atoms (29-38), the wavefront can only be controlled at wavelength scale due to the limited phase controllability of surface plasmon polaritons. In contrast, USMP-driven metasurfaces can even manipulate EM waves on deep subwavelength scale. The developed technology paves exciting ways for building multifunctional USMP-driven meta-devices with flexible access to free space, offering advantages such as ease of fabrication, reconfiguration, compatible with on-chip technology. The technology can excite many related applications such as communications, remote sensing, and virtual reality display.

Results

Phase controllability of USMPs

We first consider nonreciprocal waveguide systems that can support USMPs. The property of USMP depends on the material configuration, and two types of waveguides are investigated, as shown in Fig. 2A. One is a layered YIG-dielectric-metal structure (type-I waveguide), the other is a layered YIG-air structure (type-II waveguide). Both types of waveguides can support USMPs at microwave frequencies. Here, the dielectric in the type-I waveguide is assumed to have a relative permittivity of nearly 1 (e.g., foam). In the both waveguides, the YIG ($\epsilon_m = 15$) (39) possesses remanent magnetization $\hat{M}_m = \hat{y}M_m$, which breaks the time-reversal symmetry, enabling the existence of USMP in the absence of external magnetic field. The remanence induces gyromagnetic anisotropy in the YIG, with the permeability tensor taking the form

$$\mu_m = \begin{bmatrix} \mu_1 & 0 & -i\mu_2 \\ 0 & 1 & 0 \\ i\mu_2 & 0 & \mu_1 \end{bmatrix}, \quad (1)$$

where $\mu_1 = 1$, and $\mu_2 = \omega_m/\omega$ (ω is the angular frequency). Here, $\omega_m = 2\pi f_m = \mu_0 \gamma M_m$ is the characteristic circular frequency (μ_0 is the vacuum permeability, γ is the gyromagnetic ratio). Surface magnetoplasmons (SMPs) in the type-I waveguide have a dispersion property closely depending on the dielectric-layer thickness (d), which is described by the dispersion relation

$$\alpha_r \mu_v + \left(\alpha_m + \frac{\mu_2}{\mu_1} k \right) \tanh(\alpha_r d) = 0, \quad (2)$$

where k is the phase constant, $\alpha_m = \sqrt{k^2 - \epsilon_m \mu_v k_0^2}$ with $\mu_v = \mu_1 - \mu_2^2/\mu_1$, and $\alpha_r = \sqrt{k^2 - k_0^2}$ for $|k| > k_0$ and $\alpha_r = -i\sqrt{k_0^2 - k^2}$ for $|k| \leq k_0$. The dispersion relation for the type-II waveguide can be directly obtained from Eq. 2 by letting $d = \infty$, which gives

$$\alpha_r \mu_v + \alpha_m + \frac{\mu_2}{\mu_1} k = 0. \quad (3)$$

The linear terms with respect to k in Eqs. (2) and (3) imply that the two waveguides are intrinsically non-reciprocal, which means the possibility of unidirectional transmission.

The dispersion equation (2) for the type-I waveguide was numerically solved, and the results are displayed in Fig. 2B, where various d values were analyzed. The dispersion

relation for SMPs in the type-I waveguide only has a single branch, and it passes through the whole light cone in air. The slope of the dispersion curve is always positive, indicating that SMPs are entirely a USMP (type-I USMP). Besides, the dispersion curve descends along with increasing d , and therefore the phase constant k can be tailored by controlling air-layer thickness. For all cases, type-I USMPs have an asymptotic frequency of $\omega_{\text{smp}} = 0.5\omega_m$, which gives a lower-frequency cutoff to them. However, only within the ferrite bandgap, type-I USMP can exhibit robust unidirectional propagation (CUP), because no backward-propagating mode exists there. As a result, robust type-I USMP occurs in the frequency range $[0.5\omega_m, \omega_m]$. The dispersion relation (3) for the type-II waveguide is also illustrated in Fig. 2B, and it has two asymmetric branches, one with $k < 0$ and the other with $k > 0$. Both dispersion branches are located outside the light cone in air. The dispersion branch with $k < 0$ has an asymptotic frequency of $\omega_{\text{smp}} = 0.5\omega_m$, which gives its upper-frequency cutoff. As a result, USMP (type-II USMP) occurs in the range of $\omega_{\text{smp}} > 0.5\omega_m$. The type-II USMP is not robust against obstacle or disorder, and it will be partly scattered into free space when it meets them. Clearly, in the range of our concern $[0.5\omega_m, \omega_m]$, both types of waveguides support USMPs. In contrast to type-II USMP with $k > k_0$, type-I USMP has a phase constant k that can be tuned within the range over $[-k_0, k_0]$ by varying d . For example, at $f = 0.75f_m$, k increases from $-1.65k_0$ to $1.07k_0$ when d grows from $0.02\lambda_m$ to $0.2\lambda_m$.

Next, we consider a periodic structure that consists of alternating type-I waveguide of length a and type-II waveguide of length b , as shown in Fig. 2C. The unit cell of this structure with subwavelength length $p = a + b$ supports both types of USMPs, and such cell is referred to as bi-USMP cell in the following. Evidently, such structures with deep-subwavelength d ($\sim \lambda/30$) can be used as metasurfaces for beam deflection, which extracts waves into free space by scattering two types of USMPs at their interfaces. The extracted wave has uniformly distributed phases (φ_i) spaced by $\Delta\varphi_{\text{cl}}$, which equals to the accumulated phase of USMPs traveling over a unit cell, given by

$$\Delta\varphi_{\text{cl}} = k_1 a + k_2 b + 2\delta\varphi_{12}, \quad (4)$$

where k_1 is the phase constant of type-I USMP that is determined by d , and k_2 is the phase constant of type-II USMP. $\delta\varphi_{12}$ represents the phase shift from the coupling of two USMPs with each other, which is far smaller than π in general (fig. S1). The subwavelength period of the metasurface eliminates high-order diffractions, hence the extracted beam has a well-defined angle θ given by $\theta = \arcsin(k_x/k_0)$, where $k_x = \Delta\varphi_{\text{cl}}/p$ also known as the Bloch wavevector. Obviously, the output angle θ can be effectively adjusted by the parameter d . Based on the phase controllability of type-I USMP, such metasurfaces can offer a beam deflection angle range of nearly 180° (fig. S2). On the other hand, noting that $\Delta\varphi_{\text{cl}}$ can also be tuned by adjusting parameter a . The $\Delta\varphi_{\text{cl}}$ was numerically calculated using full-wave finite element method (FEM), and the results are shown in Fig. 2D, where $f_m = 3.587$ GHz, $f = 0.75f_m$ and $p = 20$ mm (which is smaller than one-fifth of the wavelength). Here, to reasonably characterize the phase controllability of such metasurfaces, we introduce an effective index that is $\Delta\varphi_{\text{cl}}$ scaled by $k_0 p$,

$$n_{\text{eff}} = \Delta\varphi_{\text{cl}} / (k_0 p). \quad (5)$$

As displayed in Fig. 2D, this effective index can be tuned within the range over $[-1, 1]$, validating the phase controllability of the metasurfaces.

Let's suppose an incident wavefront in free space at $z = 0$, traveling along the positive z direction. We use $U(x, 0)$ to represent the complex field across the wavefront, and it can be written as a Fourier integral

$$U(x, 0) = \int_{-\infty}^{\infty} A(k_x) \exp(jk_x x) dk_x, \quad (6)$$

where $A(k_x)$ is the spatial spectrum of the field. The consequent field $U(x, z)$ in free space ($z > 0$) can be expressed in terms of the spatial spectrum, giving

$$U(x, z) = \int_{-k_0}^{k_0} A(k_x) e^{j(k_x x + k_z z)} dk_x + \left\{ \int_{-\infty}^{-k_0} + \int_{k_0}^{+\infty} \right\} A(k_x) e^{(ik_x x - \gamma z)} dk_x, \quad (7)$$

where $k_z = \sqrt{k_0^2 - k_x^2}$ for $|k_x| \leq k_0$ and $\gamma = \sqrt{k_x^2 - k_0^2}$ for $|k_x| > k_0$. Evidently, the field $U(x, z)$ can be divided into two parts: propagating wave with $|k_x| \leq k_0$ and evanescent wave with $|k_x| > k_0$, which are represented by the first and second terms in Eq. 7, respectively. The evanescent part attenuates rapidly along z , and as a result, the field pattern in far field is mainly determined by the propagating part. Therefore, for achieving any desired free-space mode, we only need to construct initial wavefront $U_0(x)$ with a spatial spectrum lying within the region $|k_x| \leq k_0$, i.e.,

$$U_0(x) = \int_{-k_0}^{k_0} A(k_x) \exp(jk_x x) dk_x. \quad (8)$$

For such a wavefront, the phase difference of the field between any two points separated by p should be less than $k_0 p$, i.e., $-k_0 p \leq \arg\{U_0(x+p)\} - \arg\{U_0(x)\} \leq k_0 p$ (fig. S3). For our USMP-driven metasurface, the difference of adjacent extracted phases separated by the subwavelength distance p can be tuned over the range $[-k_0 p, k_0 p]$, which corresponds to the n_{eff} tune range of bi-USMP cells larger than the interval $[-1, 1]$, so it would be suffice to implement free-space propagating wave modulation. This also greatly distinguishes with the existing metasurfaces which necessitate phase shifts cover the entire 2π phase range to achieve complete control of wavefront.

In the USMP-driven metasurfaces, the scattering strength of USMPs is determined by the mismatching between the modal profiles of two USMPs. The modal spot of type-I USMP is closely dependent on d , so the amplitude of the extracted wave can be adjusted by controlling d . Besides, the amplitude of the extracted wave can be critically affected by the size of the radiation aperture, which is characterized by the length b . From Fig. 2D, we can see that for arbitrary desired phase (n_{eff}), b can be chose from a wide range $[0, 0.78p]$, giving plenty of operational freedom for amplitudes. Therefore, by properly choosing d and a , we can simultaneously achieve desired extracted phases and amplitudes. The metasurfaces for deflecting beam directly from guided waves are commonly known as leaky-wave antennas, which typically have uniform electromagnetic responses. However, by constructing nonuniform periodic structures, where bi-USMP cells of subwavelength length p have different d and a values, we can realize spatial-variant optical responses that extract and mold USMPs to any desired free-space optical modes. Therefore, the existing technology of leak-wave antennas can be regarded as a special case of the generalized formalism for USMP-driven metasurfaces.

To show the capability of the USMP-driven metasurfaces, we numerically demonstrated Bessel-beam generation and wave focusing in free space directly from USMPs. For simplicity, we use YIG material with remanence to construct metasurface cells, which can support USMPs at microwave frequencies without external magnetic field. Besides, by using USMP cells to construct a ring cavity, vector optical vortices can be generated with quantized orbital angular momentums (OAMs). Moreover, the OAM order of radiated vortex beam can be tuned at a fixed frequency through not only adjusting the dielectric-layer thickness but also tailoring external magnetic field applied in the cavity.

Bessel-beam generation and wave focusing

Bessel beams are solutions of the free-space Helmholtz equation and have transverse amplitude distributions that are described by the Bessel functions of the first kind. Such beams have startling properties such as non-diffraction and self-reconstruction. The central spot radius of Bessel beams can be extremely narrow, on the order of one wavelength. Ideal Bessel beams are not spatially limited and carry infinite energy. The central intense region is surrounded by rings, with each ring containing an energy flux equal to that of any other. Since optical systems always have a finite aperture, Bessel beams can be only approximated in a finite region by the superposition of multiple plane waves. These beams can be achieved using axicons (i.e., conical prisms) that symmetrically refract light rays toward the optical axis, as sketched in Fig. 3A. Metasurfaces have also been used to generate Bessel beams and they are termed meta-axicons. However, most of these meta-axicons are driven by waves in free space, which makes it difficult for further on-chip integration. Here, using USMP-driven metasurfaces, we are able to generate Bessel beams directly from photonic integrated components.

As a proof of concept, we numerically demonstrate the generation of two-dimensional (2D) zero-order Bessel beam using a USMP-driven meta-axicon (Fig. 3B). Such a meta-axicon requires a spatial phase profile of the form

$$\phi(x) = -\alpha|x|, \quad (9)$$

where $\alpha = k_0 \sin \theta$ is the transverse wave number, and θ is the angle at which radiation rays cross the optical axis (Fig. 3B). For a meta-axicon with length L , it consists of $(2N+1)$ bi-USMP cells of the same length $p = L/(2N+1)$, where p is much smaller than the designed wavelength. The cells are characterized by the geometric parameters a_n , d_n and $b_n = p - a_n$, where $n \in [-N, N]$. These cells can create radiation at positions $x_n = np$, and the phase difference ($\Delta\phi_n$) between the radiations at x_n and x_{n-1} is determined by a_n and d_n , as described by Eq. 4, i.e., $\Delta\phi_n = \Delta\phi_{cl}(a_n, d_n)$. According to (9), it is required that $\Delta\phi_{cl}(a_n, d_n) = \alpha p$ for $n \leq 0$ and $\Delta\phi_{cl}(a_n, d_n) = -\alpha p$ for $n > 0$. To achieve a uniform-intensity extraction, the extraction efficiency (η_n), which is defined as the ratio of the radiation power to the incident power for each cell, should increase along the x axis to balance with the propagation loss of USMPs. Assuming that the attenuation of USMPs mainly originates from the extraction loss, then the extraction efficiency of the n -th cell should be

$$\eta_n = \eta_{-N} \left/ \prod_{n'=-N}^{n-1} e^{-\eta_{n'}} \right. \approx \eta_{-N} \left/ \prod_{n'=-N}^{n-1} (1 - \eta_{n'}) \right.. \quad (10)$$

Thus, all the parameters a_n and d_n can be determined from $\Delta\phi_n$ and η_n in a step by step manner. Simulated electric field distribution for the designed meta-axicon validates that the extracted waves have uniform amplitudes and spatial-variant phases as described by Eq. 9 (Fig. 3C).

The Bessel beam generated by the USMP-driven meta-axicon is numerically simulated using full-wave FEM. Figures 3D and 3E show simulated amplitude profile of the nonzero field components E_y and H_z at the designed frequency $f = 2.69$ GHz. The field pattern of H_x is almost identical to that of E_y . The propagation range of the Bessel beam is observed to be $y_{max} = 365$ mm. This maximum propagation length is close to the theoretical value using geometric optics, that is $L/(2\tan\theta) = 467.65$ mm, where $L = 540$ mm is the length of the meta-axicon region. Figures 3F and G show the field component amplitude along the horizontal lines indicated in Figs. 3D and E, respectively. The transverse distribution of E_y agrees well with the zero-order Bessel function $J_0(\alpha x)$, where $\alpha = k_0 \sin \theta$. The full width at half maximum (FWHM) of this Bessel beam is 54.6 mm, which is close to its theoretical value, given by $\omega_{FWHM} = 2.25/\alpha = 79.87$ mm. In addition, the transverse distribution of H_z matches the first-order Bessel function $J_1(\alpha x)$, and this is similar to the situation of three-

dimensional (3D) Bessel beam with linear polarization. To examine whether the Bessel beam generated by our meta-axicon has the self-construction property, we place a metallic rod (with diameter $D = \lambda/2$) at $y = 100$ mm in the central region of the beam. The simulated E_y field is displayed in Fig. 3J. The field pattern behind the obstruction is not greatly changed. Evidently, the central region of the Bessel beam keeps its constant size and intensity because energy is diffracted into this region from its side lobes. As a result, no shadow of the object blocking the beam is observed after a short spatial interval.

It should be noted that 2D Bessel beams are not exact solutions of the free-space Helmholtz equation. Therefore, 2D fields can only exhibit approximate form of Bessel beams within a very finite region. According to geometric optics, when the axicon has a larger aperture size, the generated beam would attain a larger propagation range. We theoretically calculated the free-space field propagated from a large incident wavefront with an axicon phase function described by Eq. 9, and the obtained results are displayed in Fig. 4. In the predicted propagation range, the field is extremely nonuniform, and the central spot even becomes weaker than the side lobes at the midway. Obviously, in such a larger propagation range, the propagating field is incapable to behave as a Bessel beam.

Except for 2D wavefront modulations, unidirectional guided wave-driven metasurface to realize more complex 3D manipulation of free-space wave have been further demonstrated. By simply terminate 2D bi-USMP cell in the y direction with a pair of metal slabs separated by a subwavelength distance [which can be approximated as a perfect electric conductor (PEC) in the microwave regime], 3D unidirectional guided wave-driven metasurface can be constructed (Fig. 5A). Along the x axis, the 3D USMP-driven metasurface is physically identical to the 2D one. To further realize arbitrary 3D modulation of extracted wave, initial phase along the y axis $\phi(0, j)$ should be fully controllable. Evidently, through tailor the height of the first upper metal slabs $d(1, j)$ to realize different gradual phase accumulation from the propagation of USMPs, the arbitrary initial phase of extracted wave $\phi(0, j)$ can be achieved. At any rate, based on the unique dispersion property of USMPs, through modulating the height distribution of the upper metal slabs $d\{i, j\}$, 3D bi-USMP cells can provide excellent phase controllability, resulting in extracted wave to fulfill arbitrary functions, such as 3D free-space beam directing, focusing and Bessel beam generation (Fig. 5A).

Let's take 3D beam focusing as an example. Through designing a USMP-driven metasurface to fulfill a 3D lens phase function $\phi(x, y) = -k_0(\sqrt{x^2 + y^2 + F^2} - F)$, we can focus the extracted wave in free space with a designated focal length F . Figure 5B shows the desired phase distribution $\phi(x, y)$ for realizing a 3D focusing effect with $F = 250$ mm ($\sim 2.24\lambda$) and $p = 36$ mm at 2.69 GHz. To simplify designation, the duty cycle a/p of all bi-USMP cells is fixed as 0.5. According to Eq. 4, the phase shift provided by a bi-USMP cell between the coordinates $(x-p)$ and x should be

$$\Delta\phi_{cl} = -k_0 \left[\sqrt{x^2 + y^2 + F^2} - \sqrt{(x-p)^2 + y^2 + F^2} \right]. \quad (11)$$

Evidently, based on $\Delta\phi_{cl}$, structure parameters $d\{i, j\}$ can be determined, and the meta-device can be achieved by spatially arranging 3D bi-USMP cells with the designed $d\{i, j\}$. We simulated such a metalens using a full-wave FEM at 2.69 GHz, the simulated scattered $|E_y|^2$ field distribution in both xz and yz planes is depicted in Fig. 5C. Obviously, unidirectional guided-wave is extracted and focused into free space by the metalens, with a focal length $F = 2.23\lambda$ in good agreement with theoretical prediction 2.24λ . To check the quality of the focusing effect, we quantitatively evaluate the full width at $1/e$ maximum of the focal spot on the focal plane, and find it is approximately 0.7λ (Fig. 5D). Obviously, such a value strongly depends on the aperture size of our metalens, and can be further

reduced by enlarging the total size of our metasurface. Furthermore, the simulated phase of extracted electric field agrees well with those from our theoretical calculations, along not only the x direction (Fig. 5E, top), but also the y direction (Fig. 5E, bottom), further validating our USMP-driven metasurface approach.

It is worth mentioning that, although the size of bi-USMP cell p in the above example is set as $p = 36$ mm ($\sim \lambda/3.1$) (we chose a larger p for reducing the demand for computational resources), it is also entirely feasible for the use of deep subwavelength cells. To prove this, we designed another metasurface with $p = 5$ mm ($\sim \lambda/22$) and displayed its beam focusing functionality (fig. S4). Moreover, it is important to evaluate the efficiency of the proposed metasurface (fig. S5). The simulated utilization efficiencies (UEs) of proposed metasurface is 72% for Bessel-beam generation, which is calculated as the ratio between phase-modulated output and the energy decrease of USMPs inside the waveguide, the lowered efficiency mainly originates from the loss of material absorption. In the simulation, the loss effect was studied as the damping coefficient $\nu = 10^{-3}\omega$.

Tunable ring-cavity OAM source

Using 3D bi-USMP cells to construct a ring cavity, we are able to create a tunable source that directly emits OAM beams. The OAM beams are helically phased beams comprising an azimuthal phase term $\exp(il\theta)$, and they carry an OAM of lh per photon, where l is an integer known as the topological charge, and θ is the azimuthal angle with respect to the propagation direction. Different from spin angular momentum (SAM), which is associated with photon spin and manifested as circular polarization, the OAM is linked to the spatial distribution with vortex nature. In contrast to the SAM, which can only take two values of $\pm\hbar$, the OAM is unbounded. Thus, EM waves can have an infinite number of orthogonal OAM states theoretically. Due to this unique property, OAM beams are considered as potential candidates for encoding information in both classical and quantum optical systems. A conventional system for generating OAM beams is usually based on the combination of a bulk source with additional phase-front shaping components, such as spatial phase plates, spatial light modulations, and metasurfaces. However, relying on rather different device technologies and material platforms, this approach is not easily scalable and integratable. By using USMP-driven metasurface technology, this fundamental limitation can be overcome, and compact, integratable and tunable ring-cavity OAM sources can be realized.

A ring cavity generally supports degenerate whispering gallery modes (WGMs): clockwise (CW) and counterclockwise (CCW) propagating modes (24). These modes circulate inside the cavity and carry large OAM. Because of the inversion symmetry of the cavity, the OAMs of CW and CCW eign-WGMs have opposite signs. These modes can be excited simultaneously, and consequently their carried OAMs cancel each other. Controllable OAM emission has been demonstrated by implementing a phase-gradient metasurface integrated on a ring cavity. This metasurface breaks the degeneracy of two counter-propagating WGMs so that only one WGM can couple to the free space emission. Here, using bi-USMP cells to construct a ring cavity, we develop a straightforward approach to achieve controllable OAM emission. In such cavity, the inversion symmetry is intrinsically broken, and only one of either CW or CCW WGM is allowed to propagate, which is determined by the magnetization direction in the YIG materials. In contrast to the previous approach using phase-gradient metasurface, only unidirectional power circulation can occur in our cavity, which eliminates the undesired spatial hole-burning effect resulted from the interference pattern of two counter-propagating WGMs. So the targeted WGM in our ring cavity unidirectionally circulates carrying OAM through the azimuthally continuous phase evolution.

We consider a ring cavity that consists of N uniform bi-USMP cells periodically ranged along the azimuthal direction (Fig. 6A). Suppose USMPs in the cavity travel along the CCW direction. The eigen-WGM in the cavity has the feature of azimuthal resonance and, for the M th-order mode, the following condition should be satisfied

$$N\Delta\varphi_{\text{cl}} = n_{\text{eff}} k_0 N p = 2\pi M, \quad (13)$$

where n_{eff} is the effective index of the bi-USMP cell and p is the period length. In this cavity, the USMPs are coherently scattered at the locations $\theta_n = 2\pi n/N$, where $n \in [0, N-1]$, resulting in the extracted phases $\varphi_n = 2\pi n M/N$. The extracted phases increase linearly from 0 to $2\pi M$ along the ring perimeter, thereby creating a vortex beam with topological charge $l = M$. As n_{eff} can be continuously tuned over the range $[-1, 1]$ by varying frequency, the OAM order of radiated beam can vary with frequency. More importantly, n_{eff} can be tuned at a fixed frequency through varying external magnetic field applied in the YIG material, so we can achieve OAM sources with tunable topological charges. Note that only USMPs with $|n_{\text{eff}}| < 1$ can be coupled to the free space emission, which gives a limitation to the range of achievable OAM states.

Let the quantity $l = N\Delta\varphi_{\text{cl}}/2\pi$ numerically characterize the phase shift of USMPs traveling over N bi-USMP cells. This quantity corresponds to the OAM order of eigen WGM in a ring cavity that consists of N bi-USMP cells. The quantity l can be calculated using the full-wave FEM simulation for the bi-USMP cell with periodic boundary condition. In the presence of external magnetic field (H_0), the tensor components in Eq. 1 become $\mu_1 = 1 - \omega_0\omega_m/(\omega^2 - \omega_0^2)$ and $\mu_2 = \omega_m\omega/(\omega^2 - \omega_0^2)$, where $\omega_0 = 2\pi\gamma H_0$ (γ is the gyromagnetic ratio) and ω_m is the characteristic circular frequency. Figure 6B shows the l value as a function of the external magnetic field and frequency (f). Here, we assume $N = 86$, and take the parameters for the bi-USMP cell as follows: $\omega_m = 10\pi \times 10^9$ rad/s ($f_m = 5$ GHz), $p = 3$ mm, $a = 1$ mm and $d = 1.212$ mm (the dispersion relations of USMPs for type-I and type-II waveguides are displayed in the fig. S6). As the type-I USMP in the cell only exists in the range from $\omega_0 + 0.5\omega_m$ to $\omega_0 + \omega_m$, where $\omega_0 = 2\pi\gamma H_0$ (γ is the gyromagnetic ratio), the frequency region for unidirectional WGMs in the ring cavity varies with H_0 . In the colormap, some l integers are marked with stars for the frequency $f = 8.5$ GHz, and they are found to be really the OAM orders of WGMs in the corresponding cavity. The phase shift for a single bi-USMP cell is $\Delta\varphi_{\text{cl}} = n_{\text{eff}} k_0 p$, and n_{eff} can be tuned by varying H_0 over the range $[-1, 1]$. As a result, the OAM order has at least a tunable range of $[-l_{\text{max}}, l_{\text{max}}]$, where $l_{\text{max}} = \text{int}[Np/\lambda_0]$ with λ_0 being the designed wavelength. Clearly, the radiated OAM can be adjusted at a fixed frequency through varying external magnetic field H_0 . In addition, the n_{eff} value varies with frequency, and so does the OAM order l of WGM in the ring cavity. Thus, our ring cavity can output vortex beams with different OAM orders for different frequencies, as indicated in Fig. 6C, where $H_0 = 1785$ Gs. For $d = 1.212$ mm, the OAM order l can vary from -7 to 7 over the frequency range $[8.15, 9.2]$ GHz (fig. S7). Besides, it is also available for our ring source to output vortex beams with the same OAM order over a frequency range by properly adjusting the external magnetic field. Therefore, based on the nonresonant mechanism of the metasurface, our ring OAM source can operate over a wide frequency range.

To verify the controllability of the OAM emission with the external magnetic field H_0 , as marked in Fig. 6B, we displayed the simulated results of OAM radiation from the ring cavity with three representative magnetic field $H_0 = 1.92, 1.86$, and 1.57 kGs in Fig. 6D1-F3 at the designed frequency $f = 8.5$ GHz (complete results are displayed in the fig. S8). The radiated OAM beams is radially polarized. The electric field E_r has a spiral pattern, and its phase changes by $-7 \times 2\pi, -4 \times 2\pi$ and $5 \times 2\pi$ respectively upon one full circle around the center of the vortex, indicating the topological charge $l = -7, -4$ and 5 , matching our

simulation result in Fig. 6B. Moreover, the intensity of the electric fields are spatially distributed in a doughnut shape with a dark core in the center, which are due to the topological phase singularity at the beam axis, where the phase becomes discontinuous. On the other hand, according to Fig. 6C, the OAM charge can also be controlled by varying frequency f . To illustrate this, Fig. 6G1-I3 shows three OAM states of $l = -6, 2$ and 7 at frequencies $f = 8.2, 8.74$, and 9.2 GHz, which agree well with those from our theoretical calculation in Fig. 6C. Furthermore, Fig. 6C indicates that the OAM charge can also be tailored by varying structure parameter d (fig. S9).

Discussion

Our USMP-driven metasurfaces, consisting of uniform or nonuniform bi-USMP cells of subwavelength length, provide a highly versatile and compact platform for achieving free-space optical functionalities directly from surface plamonic waves. Different from existing metasurfaces with meta-atoms, which induce abrupt phase shifts in the optical path, the present metasurfaces rely on gradual phase accumulation from the propagation of USMPs to mold optical wavefront in subwavelength scale. Such metasurfaces can provide unparalleled phase controllability to free-space wave propagation based on the unique dispersion property of USMP. We have demonstrated the generation of a Bessel beam and wave focusing using these structures. In addition, by taking advantage of the unidirectional propagation of USMPs, we used a ring-cavity formed by bi-USMP cells to generate optical vortices that have a helical wavefront and carry OAM with a designable order. Besides, the dispersion property of USMPs can be flexibly tailored by either geometric parameter or external magnetic field, thus facilitating the realization of dynamic controllability of USMP-driven metasurfaces. We have also demonstrated the tunability of OAM order of radiation with the geometric parameter and magnetic field at a designed frequency. The design strategies presented in the paper allow one to tailor in an almost arbitrary way the phases and amplitudes of an optical wavefront. On the basis of the demonstrated design principle, more complex functionalities can be realized, such as USMP-driven holograms, virtual reality displays, and so forth. Furthermore, as our metasurfaces can control wavefronts at deep subwavelength scales, they are capable to realize desired fine field patterns in near field. Such near-field manipulation can break the optical diffraction limit, thus yielding important applications in optical detection, optical sensing and high-resolution optical imaging. The developed technology can be extended to higher frequency regimes and could have major implications for integrated optics (5, 40).

Materials and Methods

The theoretical data shown in Figs. 2B and D were obtained using the software of MATLAB. All numerical simulations were conducted using the finite element method (FEM), with third-order finite elements and at least 10 mesh steps per wavelength to ensure the accuracy of the calculated results. In all 2D and 3D simulations, unidirectional surface magnetoplasmons (USMPs) were excited by point sources and line currents, respectively, placed in a unidirectional waveguide which is connected to the metasurface system. The

effects of material absorption of yttrium iron garnet (YIG) were considered in the damping coefficient, which was set to $\nu = 10^{-3}\omega$, where ω is the operating angular frequency.

We simulated a periodic structure consisting of uniform bi-USMP cells (Fig. 2C) using the FEM. The phase difference between the extracted waves from two neighboring cells was calculated as $\Delta\phi$. We then systematically varied the geometrical parameters of the bi-USMP cells to obtain phase maps/contours (Fig. 2D). By analyzing the desired phase profiles, we obtained the target phase difference distribution $\Delta\phi(x, y)$. Subsequently, we identified the structural parameters that correspond to the target phase distribution by searching the phase maps. This approach allowed us to accurately determine the detailed structure of the bi-USMP cells required for achieving the desired phase distribution.

To generate free-space Bessel beams with both desired phases and amplitudes, we separately calculated phase and amplitude maps of the extracted waves for each bi-USMP cell, as they relate to the structural parameters a_i and d_i . Our objective was to obtain the required phase and amplitude of the extracted waves, which were represented as two lines in the maps. The intersection of these two lines corresponds to the values of a_i and d_i needed for each cell. The unidirectional propagation property of USMPs allows us to determine the values of a_i and d_i for each cell in a step-by-step manner, as the structural parameters of the next cell did not affect the radiation amplitude and phase of the previous one. This approach allows us to accurately determine the detailed structure of the bi-USMP cells required for achieving the desired not only phase but also amplitude distributions.

References

1. W. L. Barnes, A. Dereux, T. W. Ebbesen, Surface plasmon subwavelength optics. *Nature* **424**, 824-830 (2003).
2. J. B. Pendry, Negative Refraction Makes a Perfect Lens. *Phys. Rev. Lett.* **85**, 3966-3969 (2000).
3. M. Kauranen, A. V. Zayats, Nonlinear plasmonics. *Nat. Photon.* **6**, 737-748 (2012).
4. S. I. Bozhevolnyi, V. S. Volkov, E. Devaux, J. Y. Laluet, T. W. Ebbesen, Channel plasmon subwavelength waveguide components including interferometers and ring resonators. *Nature* **440**, 508-511 (2006).
5. L. Bi, J.-J. Hu, P. Jiang, D. H. Kim, G. F. Dionne, L. C. Kimerling, C. A. Ross, On-chip optical isolation in monolithically integrated non-reciprocal optical resonators. *Nat. Photonics* **5**, 758–762 (2011).
6. A. Hartstein, E. Burstein, A. A. Maradudin, R. Brewer, R. F. Wallis, Surface polaritons on semi-infinite gyromagnetic media. *J. Phys. C.: Solid State Phys.* **6**, 1266-1276 (1973).
7. J. J. Brion, R. F. Wallis, A. Hartstein, E. Burstein, Theory of Surface Magnetoplasmons in Semiconductors. *Phys. Rev. Lett.* **28**, 1455-1459 (1972).
8. L.-F. Shen, Y. You, Z.-Y. Wang, X. H. Deng, Backscattering-immune one-way surface magnetoplasmons at terahertz frequencies. *Opt. Express* **23**, 950-962 (2015).
9. Z.-F. Yu, G. Veronis, Z. Wang, S.-H. Fan, One-way electromagnetic waveguide formed at the interface between a plasmonic metal under a static magnetic field and a photonic crystal. *Phys. Rev. Lett.* **100**, 023902 (2008).
10. H.-B. Zhu, C. Jiang, Broadband unidirectional electromagnetic mode at interface of anti-parallel magnetized media. *Opt. Express* **18**, 6914 (2010).
11. B. Hu, Q.-J. Wang, Y. Zhang, Broadly tunable one-way terahertz plasmonic waveguide based on nonreciprocal surface magneto plasmons. *Opt. Lett.* **37**, 1895 (2012).

12. V. Kuzmiak, S. Eyderman, M. Vanwolleghem, Controlling surface plasmon polaritons by a static and/or time-dependent external magnetic field. *Phys. Rev. B* **86**, 045403 (2012).
13. X. Zhang, W. Li, X. Jiang, Confined one-way mode at magnetic domain wall for broadband high-efficiency one-way waveguide, splitter and bender. *Appl. Phys. Lett.* **100**, 041108 (2012).
14. Z.-H. Yu, Z.-Y. Wang, L.-F. Shen, X.-H. Deng, One-way electromagnetic mode at the surface of a magnetized gyromagnetic medium. *Electron. Mater. Lett.* **10**, 969-973 (2014).
15. K. L. Tsakmakidis, L. Shen, S. A. Schulz, X. Zheng, J. Upham, X. Deng, H. Altug, A. F. Vakakis, R. W. Boyd, Breaking Lorentz reciprocity to overcome the time-bandwidth limit in physics and engineering. *Science* **356**, 1260-1264 (2017).
16. N.-F. Yu, P. Genevet, M. A. Kats, F. Aieta, J. P. Tetienne, F. Capasso, Z. Gaburro, Light propagation with phase discontinuities: generalized laws of reflection and refraction. *Science* **334**, 333-337 (2011).
17. S. L. Sun, Q. He, S. Y. Xiao, Q. Xu, X. Li, L. Zhou, Gradient-index meta-surfaces as a bridge linking propagating waves and surface waves. *Nat. Mater.* **11**, 426-31 (2012).
18. X. J. Ni, N. K. Emani, A. V. Kildishev, A. Boltasseva, V. M. Shalaev, Broadband light bending with plasmonic nanoantennas. *Science* **335**, 427(2012).
19. S.-L. Sun, K.-Y. Yang, C.-M. Wang, T.-K. Juan, W.-T. Chen, C.-Y. Liao, Q. He., S.-Y. Xiao, W.-T. Kung, G.-Y. Guo, L. Zhou, D.-P. Tsai, High-efficiency broadband anomalous reflection by gradient meta-surfaces. *Nano Lett.* **12**, 6223-6229 (2012).
20. N. K. Grady, J. E. Heyes, D. R. Chowdhury, Y. Zeng, M. T. Reiten, A. K. Azad, A. J. Taylor, D. A. R. Dalvit, H.-T. Chen, Terahertz metamaterials for linear polarization conversion and anomalous refraction. *Science* **340**, 1304-1307 (2013).
21. X. Li, S.-Y. Xiao, B.-G. Cai, Q. He, T.-J. Cui, L. Zhou, Flat metasurfaces to focus electromagnetic waves in reflection geometry. *Opt. Lett.* **37**, 4940-4942 (2012).
22. X.-Z. Chen, L.-L. Huang, H. Muhlenbernd, G.-X. Li, B.-F. Bai, Q.-F. Tan, G.-F. Jin, C.-W. Qiu, S. Zhang, T. Zentgraf, Dual-polarity plasmonic metasurface for visible light. *Nat. Commun.* **3**, 1198 (2012).
23. D.-M. Lin, P.-Y. Fan, E. Hasman, L. B. Mark, Dielectric gradient metasurface optical elements. *Science* **345**, 298-302 (2016).
24. P. Miao, Z.-F. Zhang, J.-B. Sun, W. Walasik, S. Longhi, N. M. Litchinitser, L. Feng, Orbital angular momentum microlaser. *Science* **353**, 464-467 (2016).
25. G.-X. Zheng, H. Muhlenbernd, M. Kenney, G.-X. Li, T. Zentgraf, S. Zhang, Metasurface holograms reaching 80% efficiency. *Nat. Nanotechnol.* **10**, 308-312 (2015).
26. X.-X. Guo, Y.-M. Ding, X. Chen, Y. Duan, X. Ni, Molding free-space light with guided wave-driven metasurfaces. *Sci. Adv.* **6**, eabb4142 (2020).
27. Z. Li, M. H. Kim, C. Wang, Z. Han, S. Shrestha, A. C. Overvig, M. Lu, A. Stein, A. M. Agarwal, M. Lončar, N. Yu, Controlling propagation and coupling of waveguide modes using phase-gradient metasurfaces. *Nat. Nanotechnol.* **12**, 675–683 (2017).
28. Y. Meng, Y. Chen, L. Lu, Y. Ding, A. Cusano, J. A. Fan, Q. Hu, K. Wang, Z. Xie, Z. Liu, Y. Yang, Q. Liu, M. Gong, Q. Xiao, S. Sun, M. Zhang, X. Yuan, X. Ni, Optical meta-waveguides for integrated photonics and beyond. *Light: Sci. Appl.* **10**, 235 (2021).
29. H. J. Lezec, A. Degiron, E. Devaux, R. A. Linke, L. Martin-Moreno, F. J. Garcia-Vidal, T. W. Ebbesen, Beaming light from a subwavelength Aperture. *Science* **297**, 820-822 (2002).
30. N.-F. Yu, J. Fan, Q.-J. Wang, C. Pflugl, L. Diehl, T. Edamura, M. Yamanishi, H. Kan, F. Capasso, Small-divergence semiconductor lasers by plasmonic collimation. *Nat. Photonics* **2**, 564-570 (2008).
31. S. Kim, Y. Lim, H. Kim, J. Park, B. Lee, Optical beam focusing by a single subwavelength metal

slit surrounded by chirped dielectric surface gratings. *Appl. Phys. Lett.* **92**, 013103 (2008).

32. M. S. Kumar, X. Piao, S. Koo, S. Yu, N. Park, Out of plane mode conversion and manipulation of surface plasmon polariton waves. *Opt. Express* **18**, 8800-8805 (2010).
33. X.-M. Tang, L. Li, T. Li, Q.-J. Wang, X.-J. Zhang, S.-N. Zhu, Y.-Y. Zhu, Converting surface plasmon to spatial Airy beam by graded grating on metal surface. *Opt. Lett.* **38**, 1733-1735 (2013).
34. I. Dolev, I. Epstein, A. Arie, Surface-plasmon holographic beam shaping. *Phys. Rev. Lett.* **109**, 203903 (2012).
35. M. Ozaki, J. I. Kato, S. Kawata, Surface-plasmon holography with white-light illumination. *Science* **332**, 218-220 (2011).
36. Y.-H. Chen, L. Huang, L. Gan, Z.-Y. Li, Wavefront shaping of infrared light through a subwavelength hole. *Light. Sci. Appl.* **1**, e26 (2012).
37. J. Chen, T. Li, S. Wang, S. Zhu, Multiplexed holograms by surface plasmon propagation and polarized scattering. *Nano Lett.* **17**, 5051-5055 (2017).
38. T. Suhara, H. Nishihara, J. Koyama, Waveguide holograms: a new approach to hologram integration. *Opt. Commun.* **19**, 353-358 (1976).
39. D. M. Pozar, *Microwave Engineering*, John Wiley & Sons, New York (2011).
40. F. Y. Gardes, K. L. Tsakmakidis, D. Thomson, G. T. Reed, G. Z. Mashanovich, O. Hess, D. Avitabile, Micrometer size polarisation independent depletion-type photonic modulator in Silicon On Insulator. *Opt. Express* **15**, 5879-5884 (2007).

Acknowledgments

Funding: This work was supported by National Natural Science Foundation of China (Nos. 12104401, 62075197, 62101496). K.L.T. was supported by the General Secretariat for Research and Technology (GSRT) and the Hellenic Foundation for Research and Innovation (HFRI) under Grant No. 4509.

Author contributions: S.L. conceived the presented idea, and together with L.S. performed the initial analysis and simulations. Q.S. and H.Z. performed additional simulations and finalized the structures. S.L., K.L.T., J.Y., and S.S. analyzed and interpreted the data. All authors contributed to the final aspects of the theory, simulations, and discussions. L.S. wrote a first draft of the paper, which was then finalized by input from all co-authors. L.S., and K.L.T. supervised the work.

Competing interests: The authors declare that they have no competing interests.

Data and materials availability: All data needed to evaluate the conclusions in the paper are present in the paper and/or the Supplementary Materials.

Figures and Tables

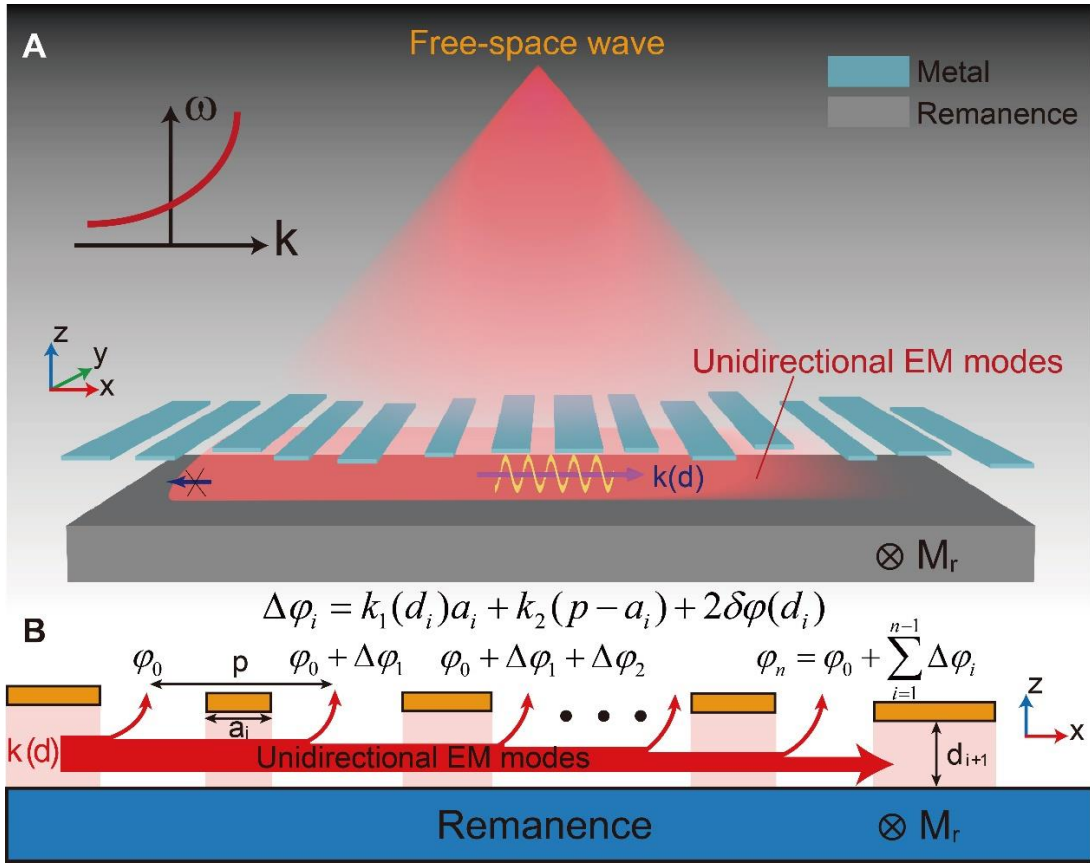


Fig. 1. Working principle of unidirectional guided-wave-driven metasurfaces. (A) Schematic of a unidirectional guided-wave-driven metasurface. The phase and intensity of the extracted wave from unidirectional waveguide by each cell can be tuned individually. An array of cells work collaboratively to form certain wavefronts and fulfill different functions, such as beam focusing. (B) Illustration of the wavefront formation of the extracted wave. The phase difference of the extracted waves from two neighboring cells is contributed from two parts: the phase accumulation $k_1(d_i)a_i + k_2(p-a_i)$ from the unidirectional guided-wave propagation and the phase shift $2\delta\varphi(d_i)$ from the coupling of two unidirectional guided modes with each other in each cell. As a result, the phase difference of the extracted waves from two neighboring cells can be expressed as $\Delta\varphi_i = k_1(d_i)a_i + k_2(p-a_i) + 2\delta\varphi(d_i)$. The superposition of phase difference $\Delta\varphi_i$ constitute the phase of extracted wave from the n -th cell $\varphi_n = \varphi_0 + \sum_{i=1}^{n-1} \Delta\varphi_i$, where φ_0 is the initial phase of the incidence.

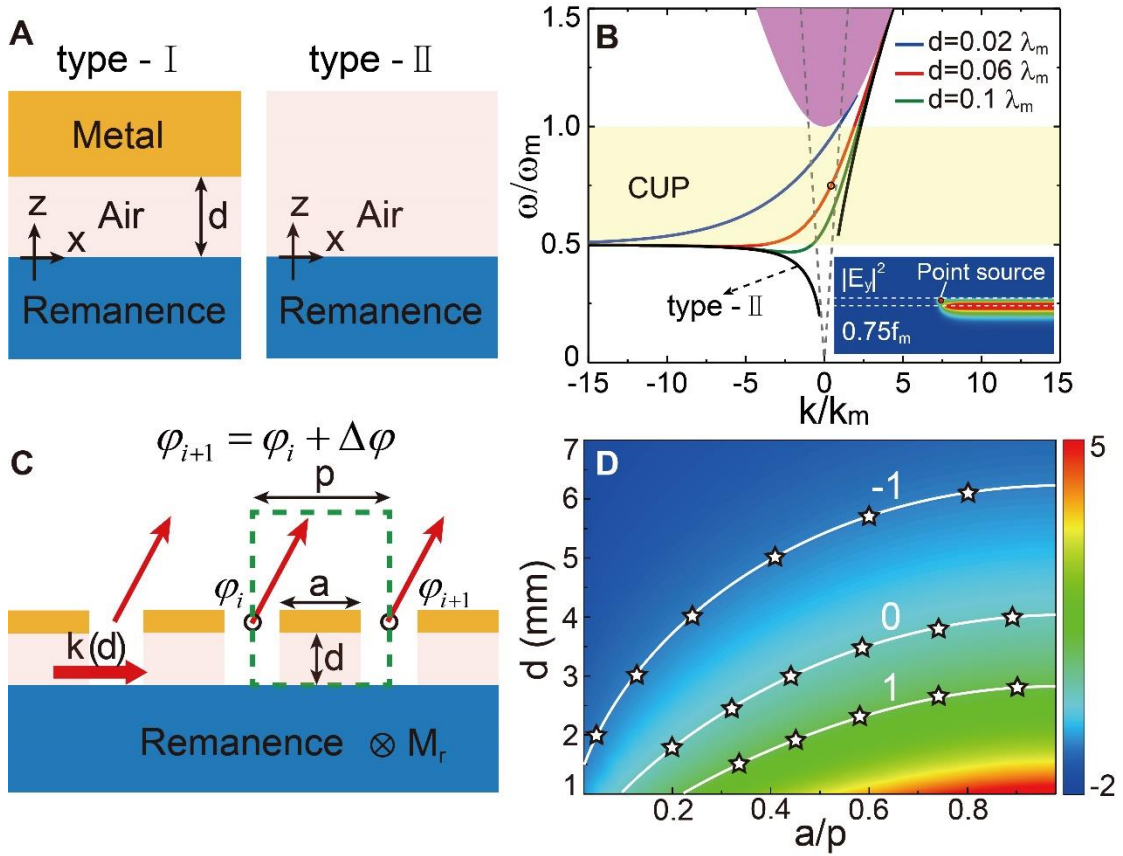


Fig. 2. Phase controllability of the unidirectional guided-wave. (A) Schematic diagram of waveguides supporting type-I and type-II USMP at microwave frequencies, and (B) the corresponding dispersion relations of USMPs for various thicknesses of the dielectric layer. The shaded rectangular area indicates the one-way region for the waveguide, and the other shaded areas indicate the zones of bulk modes in the gyromagnetic materials ($\epsilon_m = 15$). Inset: simulated electric-field intensity distribution excited by a point source placed in the middle of waveguide structure with $d = 0.06\lambda_m$ and frequency $\omega = 0.75\omega_m$. (C) Schematic picture of the uniform metasurface formed by alternating type-I and type-II waveguides shown in (A). The period length, duty cycle, and dielectric-layer thickness are denoted by p , a/p , and d respectively. The phases of extracted wave from two neighboring cells are φ_i and φ_{i+1} with a difference $\Delta\varphi$. (D) Pseudocolor map of simulated $n_{\text{eff}} = \Delta\varphi_{\text{cl}}/(k_0 p)$ for the structure of (C) in a parameter space spanned by dielectric thickness (d) and duty cycle (a/p) at 2.69 GHz. The three white lines indicate n_{eff} covering $[-1, 1]$ range with an even interval. The black stars indicate the theoretically analyzed results from Eq. 4.

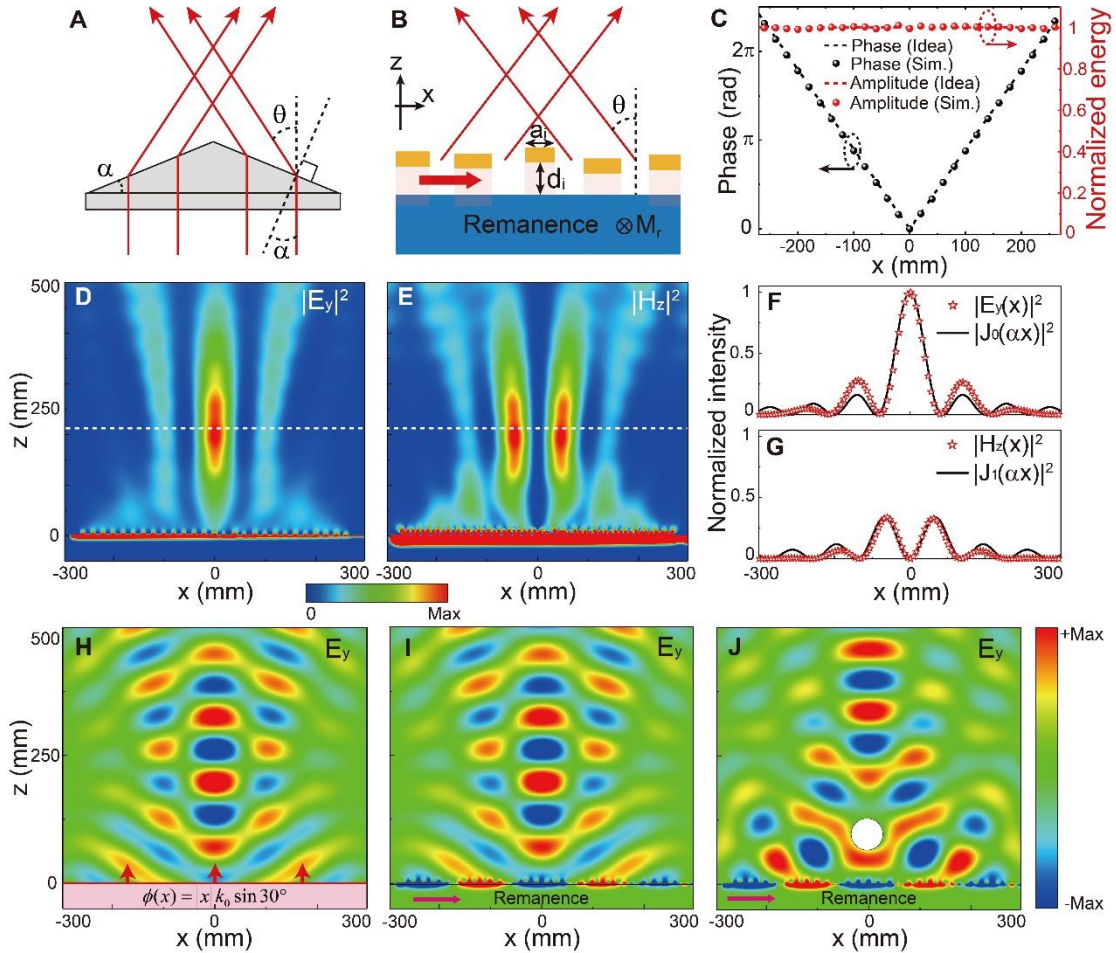


Fig. 3. Demonstration of free-space Bessel-beam generation with a unidirectional guided-wave-driven metasurface. (A) Cross-section of a 2D conventional refractive axicon comprised of a glass prism. The axicon angle α and the refraction angle θ are accordingly labeled. (B) Schematic diagram of the USMP-driven meta-axicon which is composed of nonuniform bi-USMP cells. The scattering wave from unidirectional waveguide is deflected to an angle θ toward its center to generate Bessel beam. (C) The simulated phase and energy of the extracted wave from each bi-USMP cell, and the corresponding targeted profile. (D and E) Normalized intensity profiles $|E_y|^2$ ($|H_x|^2$) and $|H_z|^2$ of the generated Bessel beam. (F and G) The horizontal cut of $|E_y|^2$ ($|H_x|^2$) and $|H_z|^2$ in (D and E), and the comparison with corresponding Bessel functions $J_0(\alpha x)$ and $J_1(\alpha x)$. (H) Theoretically computed field pattern ($\text{Re}[E_y]$) excited by an incident wavefront $E_y = \exp(-i\phi|x|)$ of finite size D at $z = 0$, where $\phi = k_0 \sin \theta$ and $\theta = 30^\circ$. (I) Simulated electric-field pattern ($\text{Re}[E_y]$) radiated from the USMP-driven meta-axicon at the frequency 2.69 GHz. (J) Field pattern ($\text{Re}[E_y]$) of the generated Bessel-beam scattered by a metallic column of diameter $\lambda/2$ placed at the height 100 mm from the metasurface.

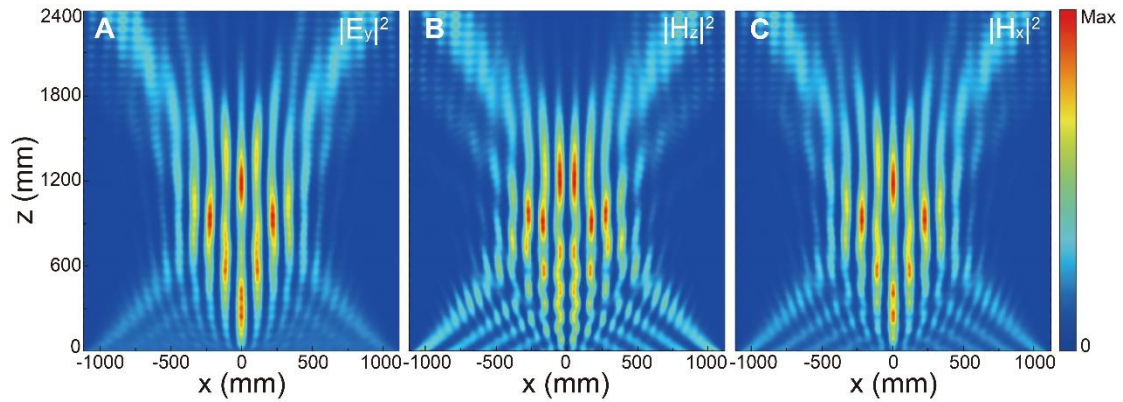


Fig. 4. Generated beam from a large incident wavefront. Propagation field in free space from an incident ideal wavefront described by the axicon phase function (9). The incident wavefront has a large size of 2230.5 mm, and the propagation range of the generated beam is evaluated to be 1932 mm using geometric optics.

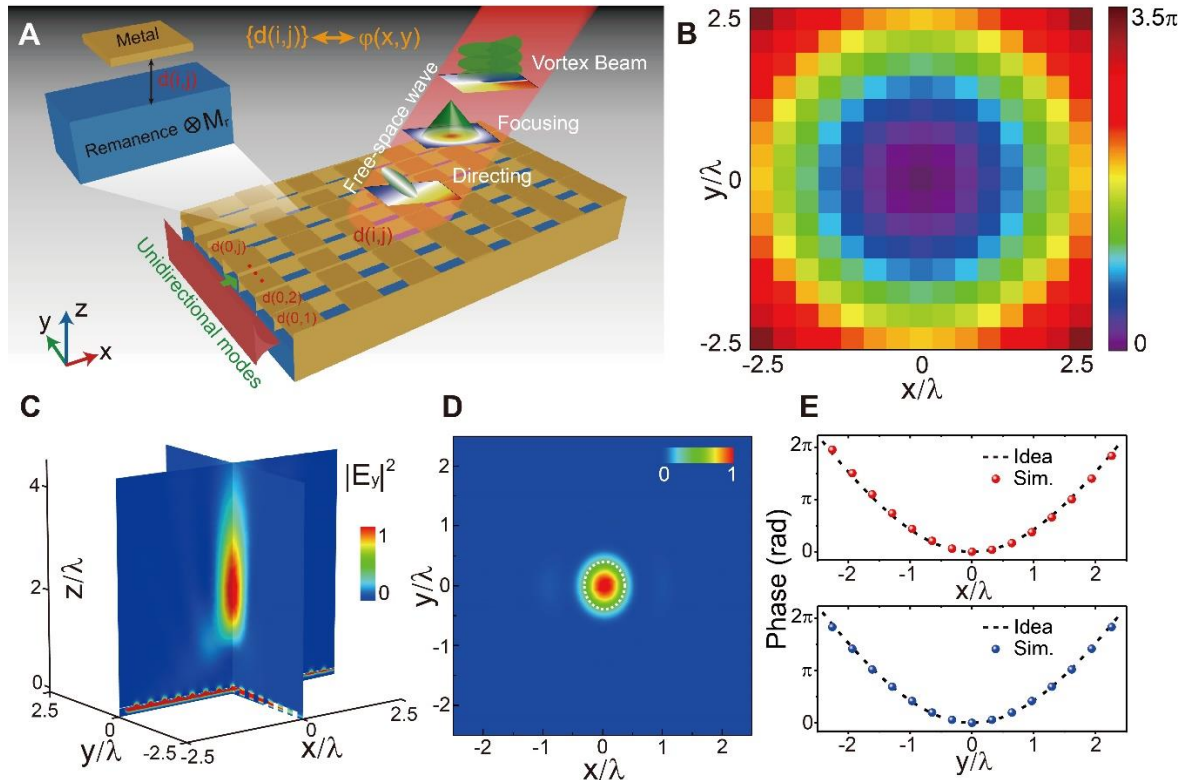


Fig. 5. Demonstration of 3D manipulation of free-space wave with a unidirectional guided wave-driven metasurface. (A) Schematic of the designed meta-device which is composed of 2D bi-USMP cells terminated in the y direction with a pair of metal slabs separated by a subwavelength distance. Through modulating the height distribution of the upper metal slabs $d\{i, j\}$, extracted wave from the unidirectional waveguide can fulfill arbitrary functions, such as free-space beam directing, focusing and vortex beam generation. (B) The phase distribution of extracted wave from each bi-USMP cells in order to realize 3D beam focusing. (C) Simulated 3D electric field intensity $|E_y|^2$ distribution of the designed meta-device, the extracted wave converged at designed focal point (2.24λ above the unidirectional waveguide) at 2.69 GHz. (D) The simulated $|E_y|^2$ distributions on the xy plane with $z = 2.24\lambda$, with the dashed-line circle defining the size of the focal spot. All field values are normalized against the maximum value in the corresponding pattern. (E) The simulated phase distribution of the extracted wave from each bi-USMP cell along x and y direction, together with the corresponding targeted profile.

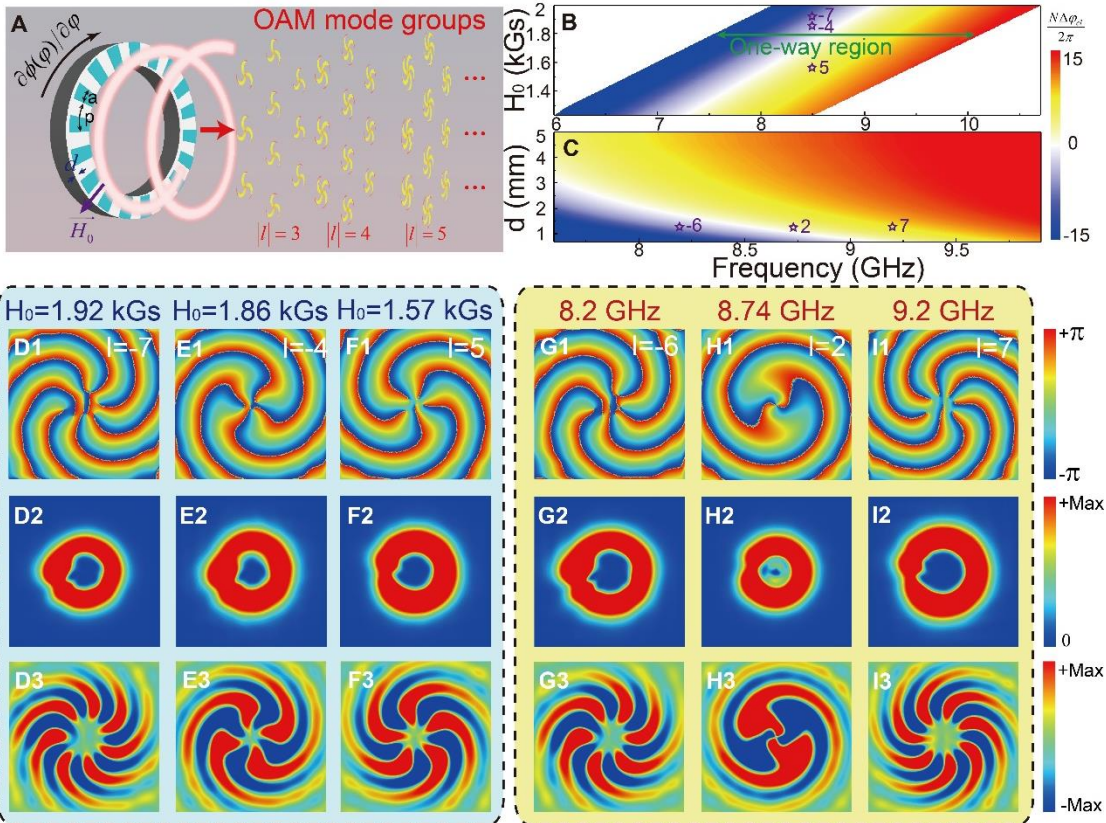


Fig. 6. Tunable ring-cavity OAM source based on the unidirectional guided wave-driven metasurface. (A) Schematic of a ring-cavity OAM source enabled by the unidirectional guided wave-driven metasurface. Unidirectional phase modulation provided by the metasurface intrinsically breaks the degeneracy of CW and CCW WGMs, leading to multiple OAM radiation at different frequencies. The dependence of USMP dispersion with geometric parameter and external magnetic field makes the radiated OAM modes tunable. (B and C) Numerical characterization of $N\Delta\varphi_{cl}/2\pi$ from the ring-cavity OAM source with varied external magnetic field (H_0) and dielectric depth (d) at different frequencies, the integer value of which corresponds to OAM with certain topological charge. (D1-F3) Simulated far-field phase, intensity and real part of E_r profiles of generated beams tuned through external magnetic field (H_0) corresponding to different OAM eigenstates, which are marked in (B). (G1-I3) The corresponding results of generated OAM beams with different eigenstates for different frequencies, which are marked in (C).

Supplementary Materials

This PDF file includes:

Sections S1 to S9

Figs. S1 to S9

Supplementary Materials for
**Broadband unidirectional guided-wave-driven metasurfaces for arbitrary
wavefront control**

Shiqing Li *et al.*

*Corresponding author. Email: lfshen@zjut.edu.cn, ktsakmakidis@phys.uoa.gr

This PDF file includes:

Figs. S1 to S9
Section S1 to S9

Supplementary Materials

1. Phase shift from the coupling between two USMPs

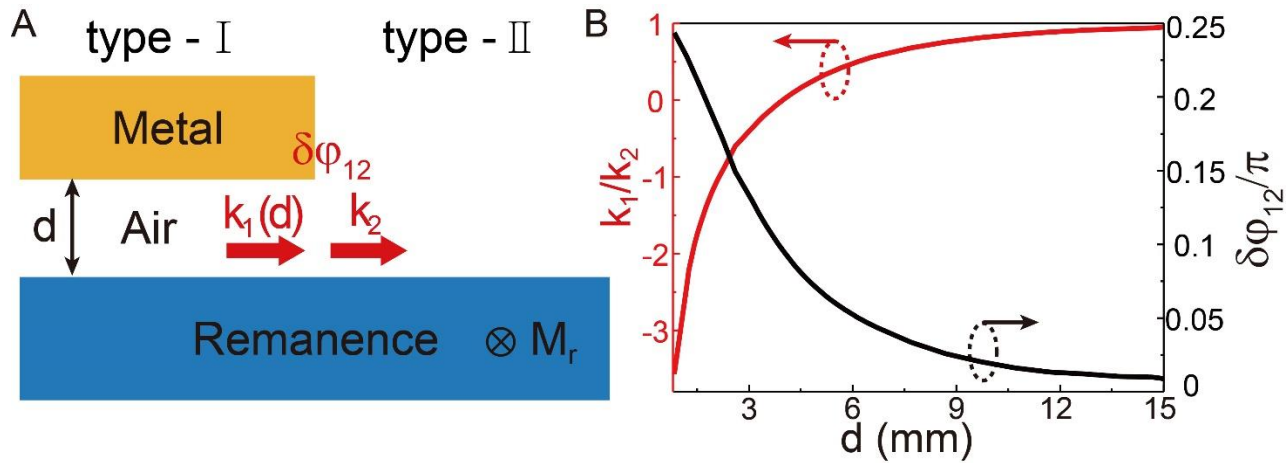


Fig. S1. Phase shift from the coupling between two USMPs. (A) Schematic diagram of the phase shift $\delta\varphi_{12}$ from the coupling between two different USMPs. (B) Simulated $\delta\varphi_{12}$ and matching degree (indicated by k_1/k_2) between the two USMPs with the variation of d . The phase shift $\delta\varphi_{12}$ increases rapidly with the mismatch between the two USMPs, and is far smaller than π in general.

2. Beam deflection with the metasurface

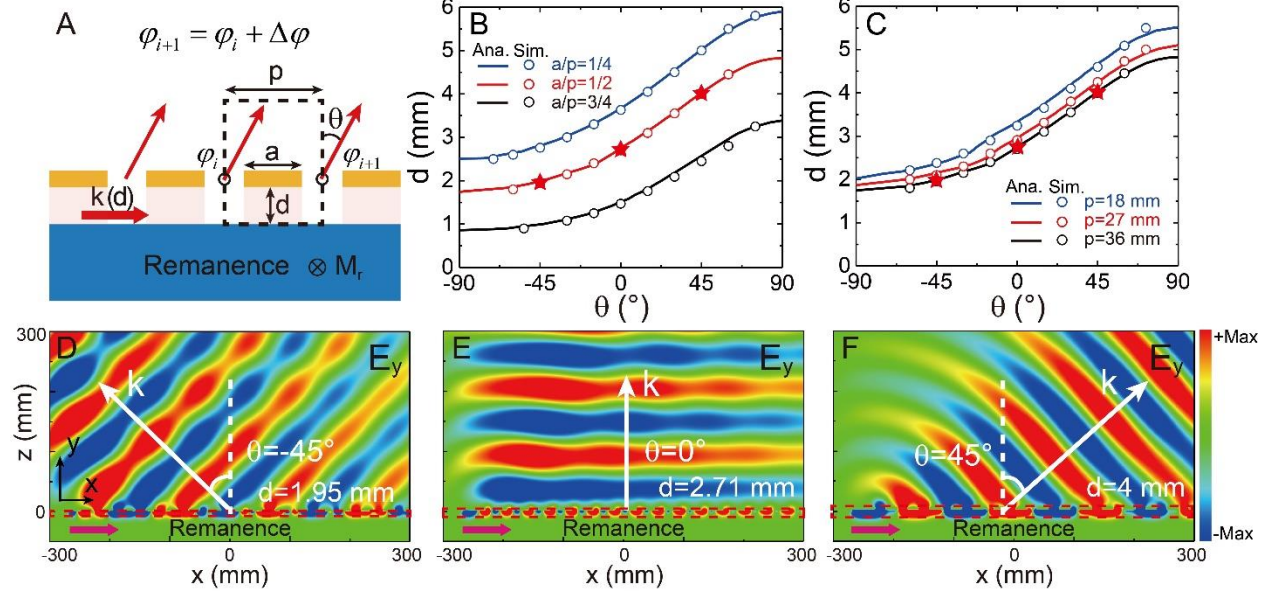


Fig. S2. Beam deflection with the metasurface. (A) Schematic diagram of the uniform metasurface formed by alternating type-I and type-II waveguides. (B, C) The analytic [solid lines, obtained by $\theta = \sin^{-1}(k_x/k_0)$] and numerical (circles) results of the radiation angle θ as a function of d . The period length is fixed at $p = 36$ mm in (B), and duty ratio is fixed at $a/p = 1/2$ in (C). (D-F) Simulated E_y field patterns radiated from the uniform metasurfaces for (D) $d = 1.95$ mm, (E) $d = 2.71$ mm, and (F) $d = 4$ mm, which are also marked by red stars in (B) and (C). In the simulations, the excited source is placed in the air layer at the left side of the uniform metasurfaces.

3. Proof of the phase inequality

In order to verify the inequality

$$-k_0 p \leq \arg \{U_0(x+p)\} - \arg \{U_0(x)\} \leq k_0 p \quad (\text{S1})$$

with $U_0(x) = \int_{-k_0}^{k_0} A(k_x) \exp(jk_x x) dk_x$, it is necessary to first prove the following basic inequality

$$\Delta\phi_{\min} \leq \left| \arg(a_1 e^{i\Delta\phi_1} + a_2 e^{i\Delta\phi_2}) - \arg(a_1 + a_2) \right| \leq \Delta\phi_{\max}, \quad (\text{S2})$$

where $\Delta\phi_{\min} = \min(|\Delta\phi_1|, |\Delta\phi_2|)$, and $\Delta\phi_{\max} = \max(|\Delta\phi_1|, |\Delta\phi_2|)$. In the proof, there are three different cases to consider: (1) $\Delta\phi_1 \geq \Delta\phi_2 \geq 0$, (2) $\Delta\phi_1 \leq \Delta\phi_2 \leq 0$, (3) $\Delta\phi_1 \geq 0, \Delta\phi_2 \leq 0$. In Fig. S3, through the graphical representation and operation of complex numbers, the following inequality is graphically obtained for case 1: $\Delta\phi_2 \leq \arg(a_1 e^{i\Delta\phi_1} + a_2 e^{i\Delta\phi_2}) - \arg(a_1 + a_2) \leq \Delta\phi_1$. In a similarly, we can obtain the inequality $\Delta\phi_1 \leq \arg(a_1 e^{i\Delta\phi_1} + a_2 e^{i\Delta\phi_2}) - \arg(a_1 + a_2) \leq \Delta\phi_2$ for case 2 ($\Delta\phi_1 \leq \Delta\phi_2 \leq 0$), and the inequality $\Delta\phi_2 \leq \arg(a_1 e^{i\Delta\phi_1} + a_2 e^{i\Delta\phi_2}) - \arg(a_1 + a_2) \leq \Delta\phi_1$ for case 3 ($\Delta\phi_1 \geq 0, \Delta\phi_2 \leq 0$). To summarize, we have proved the basic inequality (S2).

In Eq. (S2), only two pairs of complex numbers are included. Obviously, this inequality can be generalized to the general case of arbitrary (N) pairs of complex numbers, and the generalized inequality has the form

$$\Delta\phi_{\min} \leq \left| \arg\left(\sum_{n=1}^N a_n e^{i\phi_n}\right) - \arg\left(\sum_{n=1}^N a_n\right) \right| \leq \Delta\phi_{\max}, \quad (\text{S3})$$

where $\Delta\phi_{\min} = \min(|\phi_1|, |\phi_2|, \dots, |\phi_N|)$ and $\phi_{\max} = \max(|\phi_1|, |\phi_2|, \dots, |\phi_N|)$. In Eq. (S1), the complex physical quantities can also be expressed as $U(x) = \sum^N a_n$ and $U(x+p) = \sum^N a_n e^{ik_n p}$, where $a_n = A(k_n) e^{ik_n x}$ and $k_n \in [-k_0, k_0]$, therefore they satisfy the inequality (S1), i.e., $|\arg\{U_0(x+p)\} - \arg\{U_0(x)\}| \leq k_0 p$.

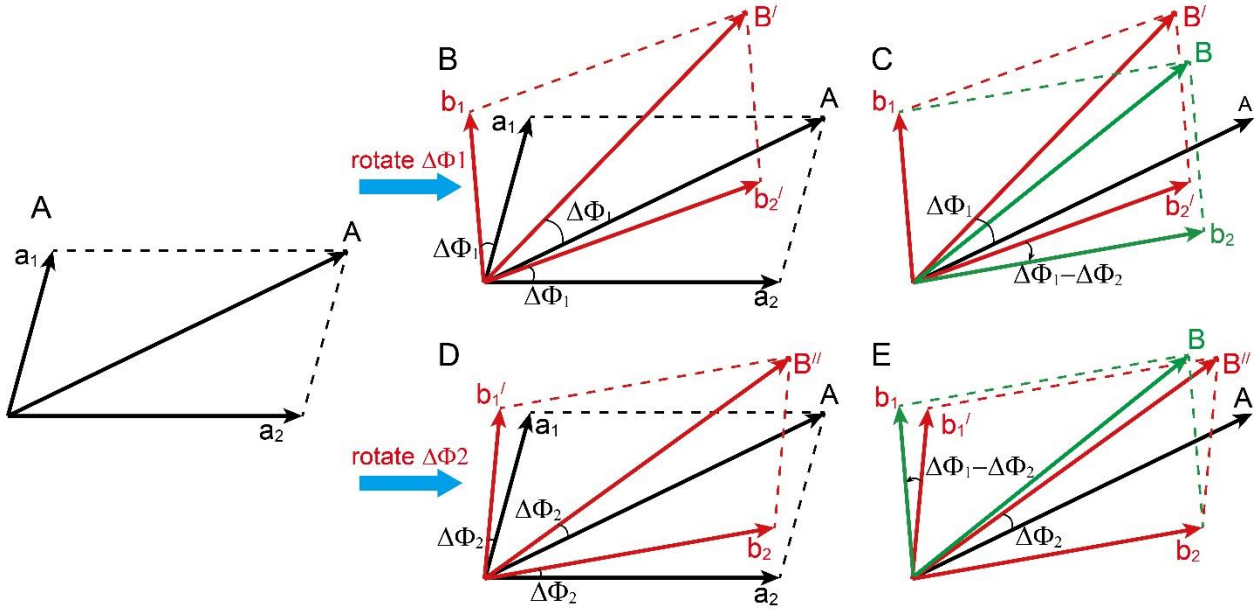


Fig. S3. Graphical representation and operation of complex numbers. We consider four complex numbers a_1 , a_2 , b_1 , and b_2 , where $b_1 = a_1 e^{i\Delta\phi_1}$ and $b_2 = a_2 e^{i\Delta\phi_2}$, and assume $\Delta\phi_1 \geq \Delta\phi_2 \geq 0$. The addition of $A = a_1 + a_2$ and $B = b_1 + b_2$ is performed graphically on the complex plane. (A) Graphically representing a_1 , a_2 , and their sum. (B) Rotating a_1 , a_2 and A together by an angle $\Delta\phi_1$, we get b_1 , b_2' and B' , respectively. (C) Dragging down b_2' by $\Delta\phi_1 - \Delta\phi_2$, we then obtain $b_2 = a_2 e^{i\Delta\phi_2}$, then add up b_1 and b_2 , we finally get B . Obviously, $\arg(B) - \arg(A) \leq \arg(B') - \arg(A)$, this means $\arg(a_1 e^{i\Delta\phi_1} + a_2 e^{i\Delta\phi_2}) - \arg(a_1 + a_2) \leq \Delta\phi_1$. (D) Rotating a_1 , a_2 and A by an angle $\Delta\phi_2$, we get b_1' , b_2 and B'' , respectively. (E) Dragging up b_1' by $\Delta\phi_1 - \Delta\phi_2$, we then obtain $b_1 = a_1 e^{i\Delta\phi_1}$, then add up b_1 and b_2 , we finally get B . Obviously, $\arg(B) - \arg(A) \geq \arg(B'') - \arg(A)$, this means $\arg(a_1 e^{i\Delta\phi_1} + a_2 e^{i\Delta\phi_2}) - \arg(a_1 + a_2) \geq \Delta\phi_2$. To sum up, we verify the inequality $\Delta\phi_2 \leq \arg(a_1 e^{i\Delta\phi_1} + a_2 e^{i\Delta\phi_2}) - \arg(a_1 + a_2) \leq \Delta\phi_1$.

4. Beam focusing with deep subwavelength cells

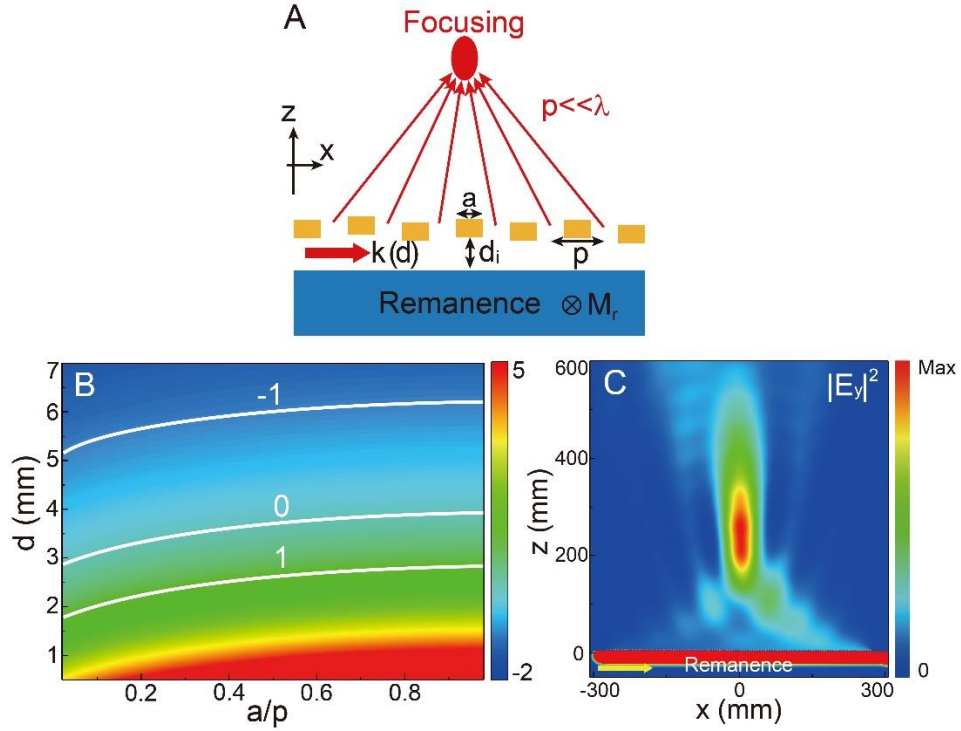


Fig. S4. Free-space beam focusing with unidirectional guided-wave-driven metasurface formed by deep subwavelength cells. (A) Schematic of the designed meta-device with deep subwavelength cells (period length $p = 5$ mm). The type-I waveguide length a is fixed at $0.5p$ for simplicity. (B) Pseudocolor map of simulated n_{eff} for structure in (A) in a parameter space spanned by air thickness (d) and duty cycle (a/p) for 2.69 GHz. The three white lines indicate n_{eff} covering $[-1, 1]$ range. (C) Simulated electric-field intensity profile $|E_y|^2$ generated by the unidirectional guided-wave-driven meta-device. The extracted wave converges at the designed focal point (250 mm above the meta-device).

5. Evaluation of efficiency of the proposed metadevices

The efficiency of the USMP-driven metasurface is evaluated and discussed in this part. Two efficiency characteristics are considered here, and they are energy efficiency (EE) and utilization efficiency (UE). The energy efficiency is defined by:

$$\text{EE} = \frac{P_{fun}}{P_{in}}, \quad (\text{S4})$$

where P_{fun} represents the output power of phase-modulated free-space wave, while P_{in} represents the input power of unidirectional guided mode in the waveguide. P_{in} and P_{fun} are obtained by integrating the energy flux over the regions s_1 and s_3 , which were marked with dotted lines in Fig. S5. The calculated EEs of designed metadevice for Bessel beam generation is 57% at the designed frequency 2.69 GHz. Evidently, the energy efficiency can be effectively improved by increasing the length of the USMP-driven metasurface in the x direction, or by connecting multiple metadevices via the unidirectional waveguide.

In order to more rationally evaluate the efficiency of USMP-driven metasurface, we introduced utilization efficiency (UE), which is defined by:

$$\text{UE} = \frac{P_{fun}}{P_l}, \quad (\text{S5})$$

where P_l represents the total power loss during the propagation of unidirectional guided modes over the metasurface. $P_l = P_{in} - P_d$, and P_d can be obtained by integrating the energy flux over the regions s_2 , which is marked with dotted line in Fig. S6. It can be seen in the main text that the energy utilization efficiency for the metadevice is 72% at the working frequency, which implies that most of the lost energy of unidirectional modes can be converted to preset free-space functionalities. Only a small part of the consumed energy is exhausted due to material absorption. Similar numerical calculations have also been done for beam focusing by our metasurfaces, and the utilization efficiency for these metalens can reach 70% after proper parameter optimization.

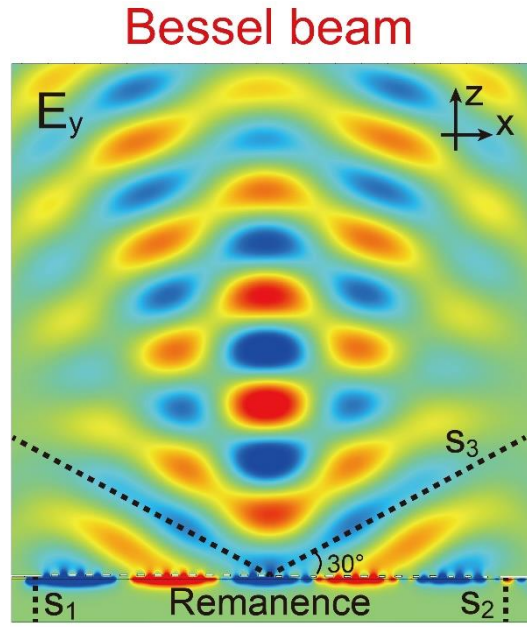


Fig. S5. The efficiency of the proposed metadevices. Simulated $\text{Re}[E_y]$ field patterns for Bessel beam generation studied in Fig. 3. The integration regions s_1, s_2, s_3 , which were marked with black dashed lines, are used to calculate the input (P_{in}) and decreased (P_d) powers of unidirectional mode, and the output power (P_{fun}) in free space, respectively.

6. The dispersion relations of unidirectional modes in the presence of external magnetic field

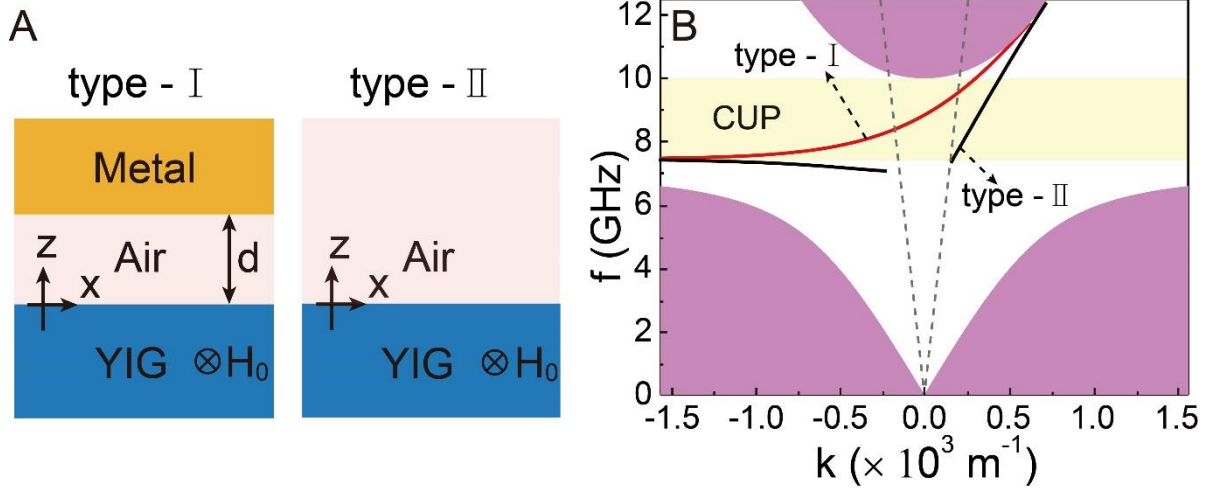


Fig. S6. The dispersion relations of unidirectional modes in the presence of external magnetic field. (A) Schematic diagram of waveguides supporting type-I and type-II USMP in the presence of external magnetic field (H_0) and (B) their corresponding dispersion relations. Here, $\omega_m = 10\pi \times 10^9$ rad/s ($f_m = 5$ GHz), and $H_0 = 1785$ Gs.

7. The generated OAMs with different orders at different frequencies

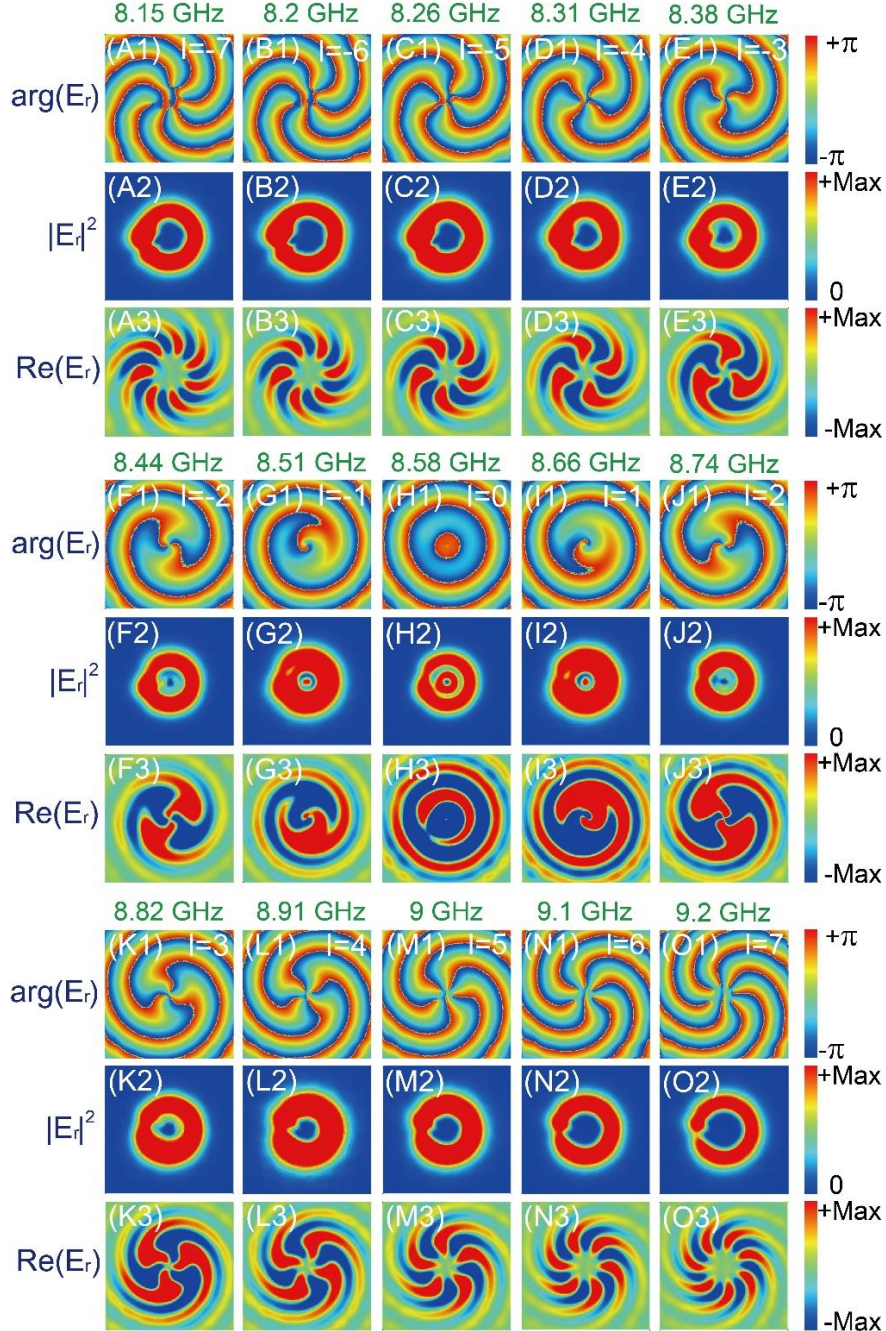


Fig. S7. The generated OAMs at different frequencies. Simulated (A1-O1) phase distributions, (A2-O2) intensity profiles, and (A3-O3) radial electric-field components of emitted OAM states at different frequencies. The ring cavity is composed of 86 bi-USMP cells with $p = 3$ mm and $a = 1$ mm. The external magnetic field is fixed at $H_0 = 1785$ Gs. The resulting topological charge of the OAMs radiation can be seen by the number of 2π phase evolution along the circumference, which ranges from -7 to $+7$ for the considered frequency range [8.15, 9.2] GHz.

8. The generated OAMs tuned through external magnetic field (H_0)

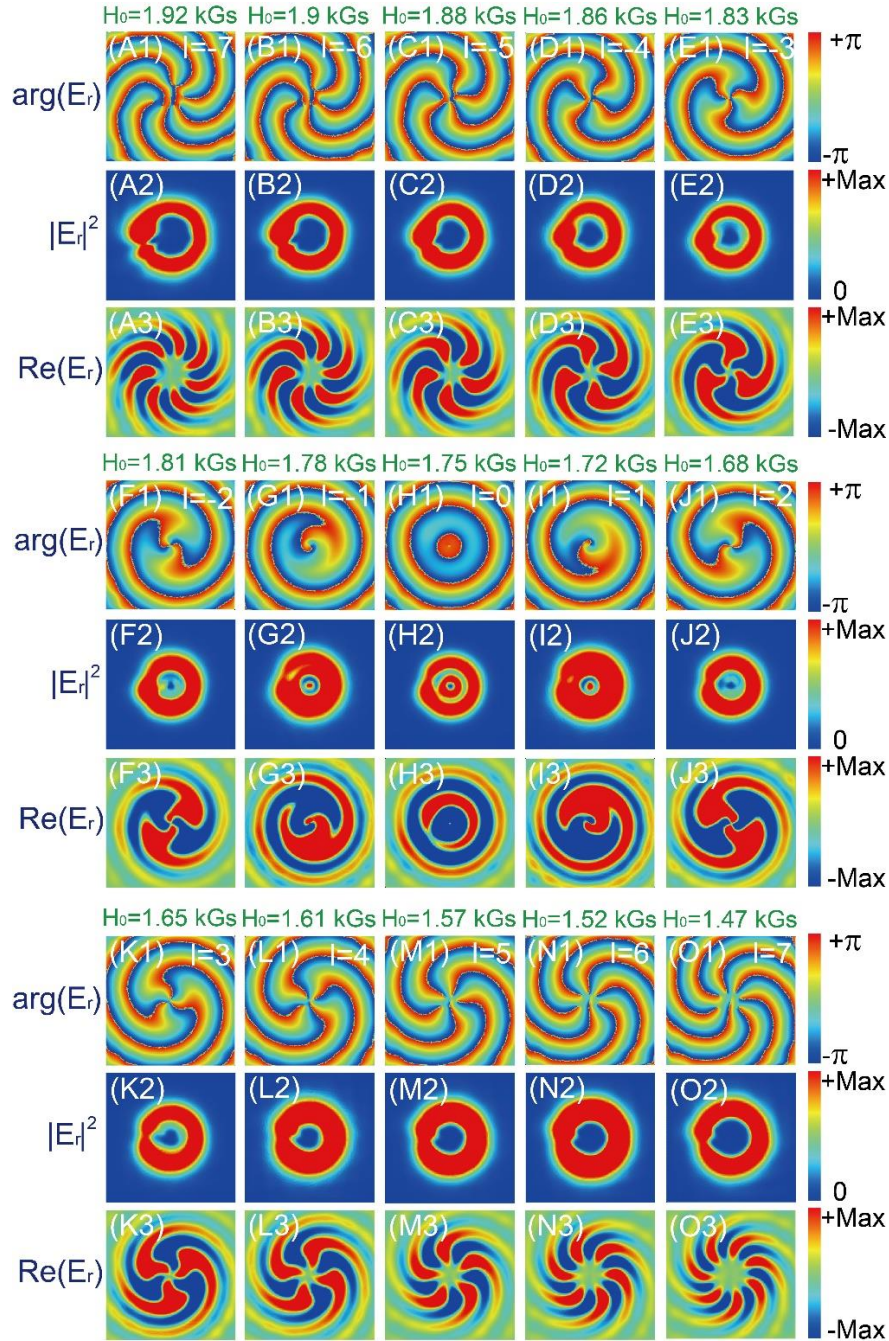


Fig. S8. The generated OAMs tuned through external magnetic field. Simulated (A1-O1) phase distributions, (A2-O2) intensity profiles, and (A3-O3) radial electric-field components of emitted OAM states for various external magnetic fields (H_0). The ring cavity is composed of 86 bi-USMP cells with $p = 3$ mm and $a = 1$ mm. The frequency is fixed at $f = 8.5$ GHz. The resulting topological charge of the OAM radiation can be seen by the number of 2π phase evolution along the circumference, which ranges from -7 to $+7$ for the H_0 tune range $[1.47, 1.92]$ kGs.

9. The generated OAMs tailored by varying structural parameter

According to Fig. 6(C), the OAM order of emitted vortex beam can also be tailored by varying structural parameter d . To verify this, Fig. S9 shows the emitted OAM states for different parameter d at $f = 8.5$ GHz and $H_0 = 1785$ Gs. The topological charge of the OAM state can be tuned from $l = -7$ to $+7$ by choosing different d values, which agrees well with our theoretical calculation shown in Fig. 6C.

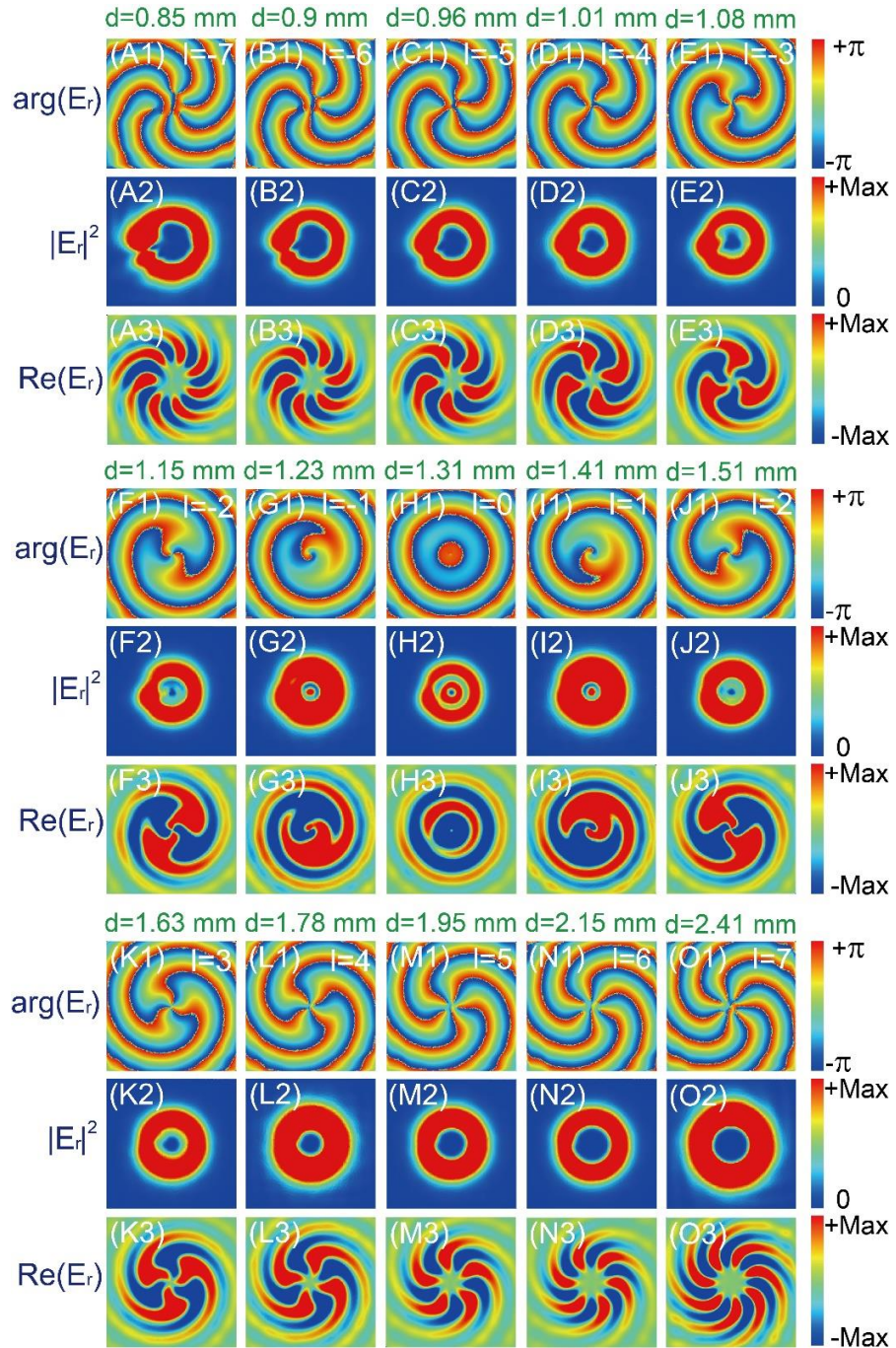


Fig. S9. The generated OAMs tailored by varying structural parameter. Simulated (A1-O1) phase distributions, (A2-O2) intensity profiles and (A3-O3) radial electric-field components of emitted OAM states tuned through the structural parameter d . The ring cavities are composed of 86 bi-USMP cells with $p = 3$ mm and $a = 1$ mm. The frequency is fixed at $f = 8.5$ GHz and external magnetic field $H_0 = 1785$ Gs. The resulting topological charge of the OAMs radiation can be seen by the number of 2π phase evolution along the circumference, which ranges from -7 to $+7$ for the chosen d values, matching well with the results in Fig. 6C.